Spatial Control of Heterogeneous Nucleation on the Superhydrophobic Nanowire Array

*Ching-Wen Lo, Chi-Chuan Wang, and Ming-Chang Lu**

Condensation is a common phenomenon and is widely exploited in power generation and refrigeration devices. Although drop-wise condensation offers high heat and mass transfer rates, it is extremely difficult to maintain and control. In this study, the ability to spatially control heterogeneous nucleation on a superhydrophobic surface by manipulating the free energy barrier to nucleation through parameterizing regional roughness scale on the Si nanowire array-coated surface is reported. Water vapor preferentially condenses on the designed microgrooves on the Si nanowire surface and continuous shedding of the drop-wise condensate is observed on the surface. The nucleation site density can also be manipulated by tailoring the density of the microgroove on the surface. Moreover, the cycle time on the Si nanowire array with microgrooves is approximately ten times smaller than that on a plain Si surface. This suggests that potentially high heat and mass transfer rates can be achieved on the surface. The insight from this study has implications in enhancing energy efficiency in a wide range of thermal energy conversion systems.

1. Introduction

Water vapor condensation is a common phenomenon in daily life and plays an essential role in distillation,[1] water harvesting,[2] power and refrigeration cycles,[3] and thermal management.[4,5] Condensation involves heterogeneous nucleation and growth of liquid droplets on a cooled surface. Heterogeneous nucleation can form either Cassie-type[6] or Wenzel-type[7] droplets on a surface. Cassie droplets are suspended on top of structures on a solid surface, whereas Wenzel droplets retain intimate contact with a solid surface. Cassie droplets which lead to drop-wise condensation (DWC) are preferred because the liquid droplets can be effectively removed from the surface, enhancing the rates of heat and mass transfer significantly.[8] However, it is difficult to maintain Cassie droplets on a surface because the Cassie state is metastable and a transition from the Cassie to Wenzel state is often observed as the driving force (e.g., temperature difference or pressure difference) increases.[9–11] Superhydrophobic surfaces are highly hydrophobic with a liquid contact angle of approximately 150° or larger.[9,10,12,13] Consequently, superhydrophobic surfaces promote Cassie droplets.[10,12–17] While the loss of superhydrophobicity under condensation has been observed on one-tier microstructured surfaces,[18–20] sustainable DWC has also been reported on two-tier nano/microstructured surfaces.[21–23] The reason behind this is presumably due to the similar scale of the smallest droplets and the nanoscale roughness on the two-tier roughened surfaces.[10] Heterogeneous nucleation is an intrinsically random process because the energy barriers to nucleation on an ordinary surface are randomly distributed. Although Varanasi et al. demonstrated the spatial control of heterogeneous nucleation of water on a surface with hydrophobic and hydrophilic segments,[24] Wenzel droplets appear on the surface and are difficult to remove. This would result in an appreciable decline of heat and mass transfer performance on such surfaces. Here, we report the ability to spatially control heterogeneous nucleation with rapid and continuous shedding of the condensate on a superhydrophobic surface. The control was achieved by means of engineering free energy barriers to nucleation through parameterizing regional roughness scales on a silicon nanowire (SiNW) array-coated surface. To the best of authors' knowledge, such an ability has never been reported. The main contribution of this work includes: 1) spatial control of heterogeneous nucleation. Water droplets with a large contact angle (approximately 145°) preferentially nucleate on the patterned microgrooves (MGs) of the SiNW array-coated surface; 2) the control of nucleation density. The nucleation site density on the MG/SiNW surfaces can be manipulated by tailoring the number of the grooves on the surface; 3) the enhancement of condensate shedding efficiency. The condensate can be rapidly and continuously shed from the superhydrophobic surfaces. The cycle time (i.e., the time required to complete a cycle from droplet nucleation to droplet departure) on the MG/SiNW surface is ten times smaller than that on a plain silicon surface. It implies potentially high heat and mass transfer rates on the MG/SiNW surface. This study opens up a new direction towards manipulating the daily phenomenon of condensation. The insight from this study has implications in enhancing efficiencies in a wide range of systems involving condensation.

The scanning electron microscope (SEM) pictures of the SiNW surface and MG/SiNW surfaces are shown in **Figure 1**.

C.-W. Lo, Prof. C.-C. Wang, Prof. M.-C. Lu
Department of Mechanical Engineering
National Chiao Tung University
Hsinchu, Taiwan, 300
E-mail: mclu@mail.nctu.edu.tw

DOI: 10.1002/adfm.201301984

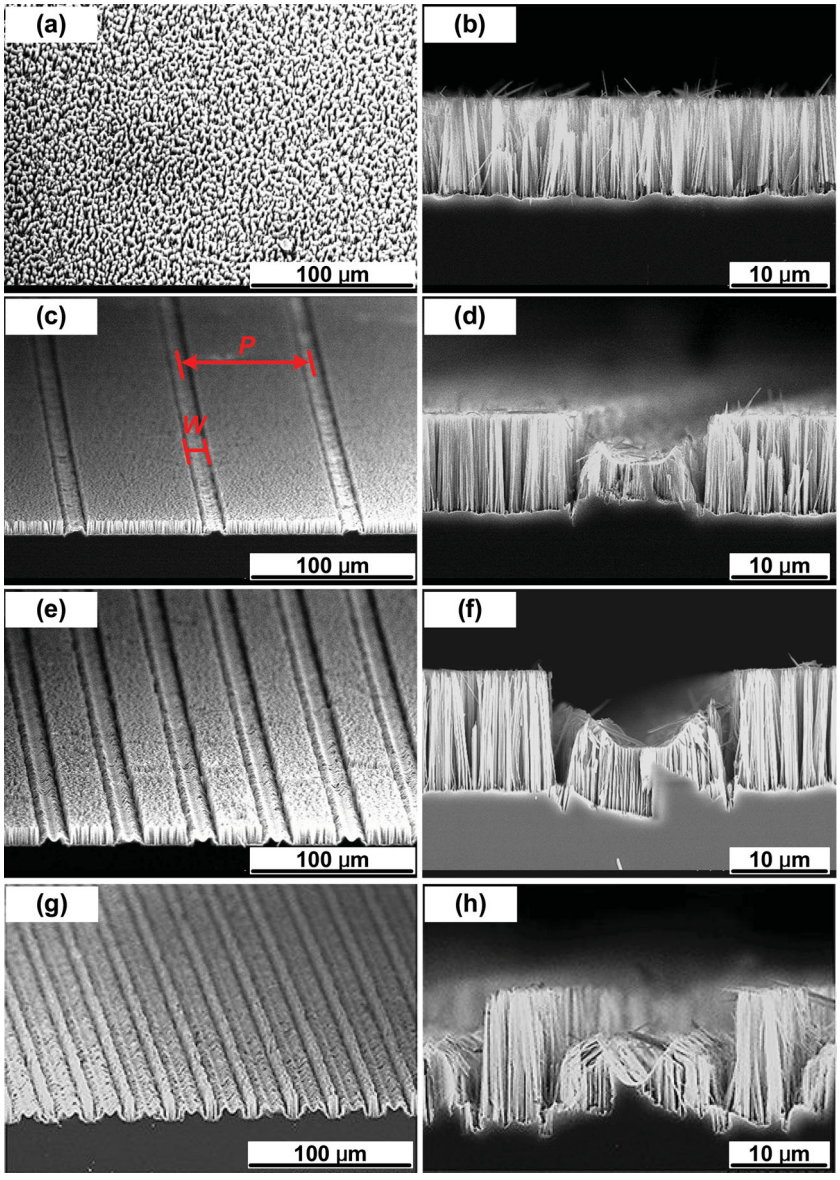

Figure 1. Scanning electron microscope (SEM) pictures (15 kV acceleration voltage) of: a) top view of SiNW surface, b) cross-section of SiNW surface, c) top view of P85 surface, d) cross-section of P85 surface, e) top view of P45 surface, f) cross-section of P45 surface, g) top view of P25 surface, and h) cross-section of P25 surface. 500× magnification in (a,c,e,g); 3k× magnification in (b,d,f,h).

The fabrication of the surfaces follows the procedure provided in the Experimental Section. Figures 1a,b show the top view and cross-sectional view of the SiNW surface, respectively. Figures 1c,e,g show the top views of the MG/SiNW surfaces with a constant groove width (W) of 15 μm with various groove pitches (P) of 85 μm, 45 μm, and 25 μm, respectively (denoted as P85, P45 and P25 surfaces hereafter). Figures 1d,f,h show the corresponding cross-sectional views of the P85, P45, and P25 surfaces, respectively. Nanowires having diameters in the range of 20–300 nm of approximately 10 μm long were synthesized for the condensation experiments. The equilibrium, advancing, and receding contact angles on the SiNW surface and the MG/SiNW surfaces are shown in Figure S1 in the Supporting Information. The equilibrium contact angles on the SiNW surface and the MG/SiNW surfaces were all about 145°. The SiNW and MG/SiNW surfaces showed a small contact angle hysteresis (i.e., the difference between advancing and receding contact angles) of approximately a few degrees. Moreover, the contact angle on the MG/SiNW surfaces is independent of the groove pitch and groove density.

It is worth noting that the large ratio between nanowire height and nanowire spacing on the synthesized SiNW and MG/SiNW surfaces can promote superhydrophobicity.[25,26] Although, the relatively large spacing between nanowires in the microgrooves on the MG/SiNW surfaces may affect superhydrophobic behavior for small droplets which are comparable in size with the spacing,[26] the sizeable cavities in the microgrooves can enhance nucleation. In the meantime, the superhydrophobicity can be recovered when the size of the droplets is comparatively larger than the spacing between nanowires in the microgrooves during condensation.

2. Results and Discussion

2.1. Visualization of Drop-wise Condensation Under ESEM

The dynamics of the water vapor condensation processes on these surfaces was investigated using the FEI Quanta 200 environmental scanning electron microscope (ESEM). The experimental details for conducting the condensation experiments in the ESEM chamber are provided in the Experimental Section. The condensation processes on these surfaces are shown in **Figure 2**. The figure also shows the condensation of water vapor on a hydrophobic plain silicon surface as a control experiment. The hydrophobic plain silicon surface was obtained by coating a thin layer of polytetrafluoroethylene (approximately 20 nm) on top of the plain silicon surface. The contact angle on the hydrophobic plain silicon surface is approximately 100° (see Figure S1 in the Supporting Information). It is also noted that a large contact angle hysteresis of approximately 80° is observed on the plain silicon surface. Figures 2a–e show the condensation processes on the plain silicon, SiNW, P85, P45, and P25 surfaces, respectively. The times shown in the rows of columns in the figure were measured from the first recordable stage of the condensation processes on these surfaces (i.e., the first row of the columns in the figure). The spatial control of heterogeneous nucleation on

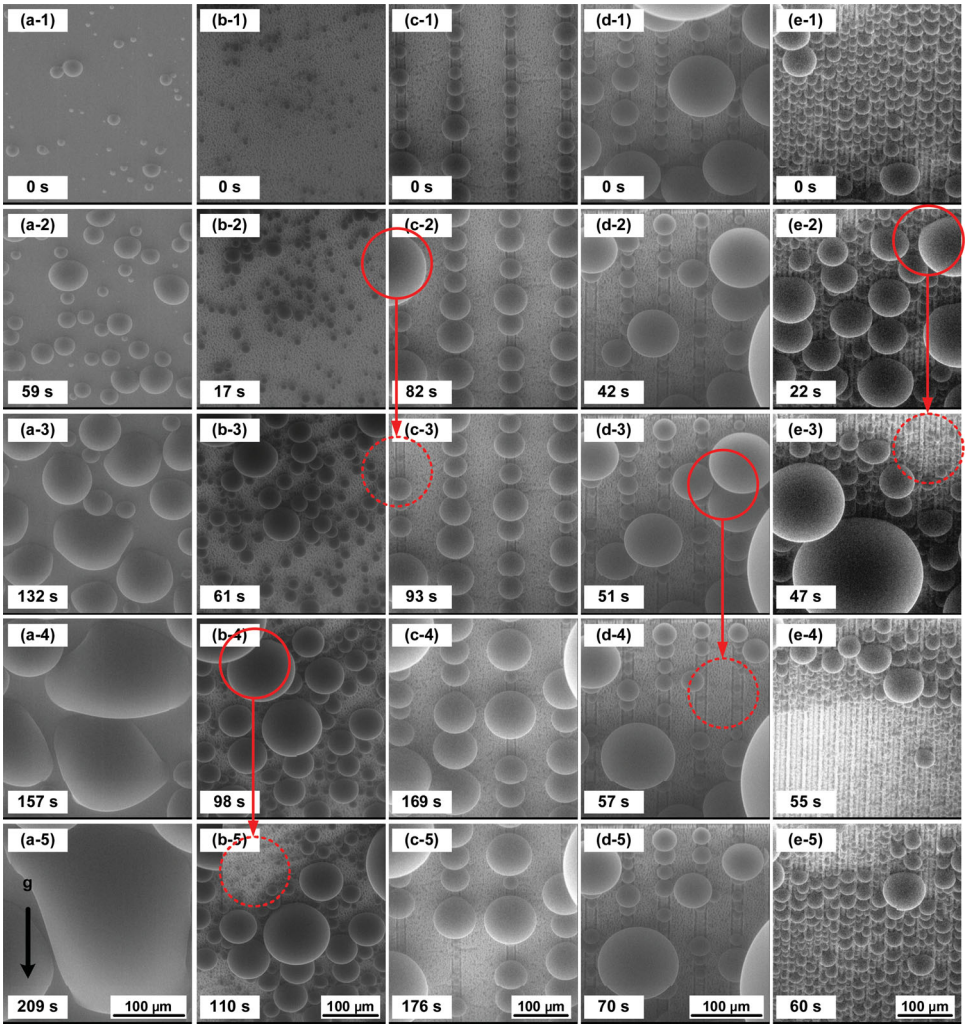

Figure 2. Environmental scanning electron microscope (ESEM) images (15 kV acceleration voltage) of the condensation processes on a) plain silicon surface, b) SiNW surface, c) P85 surface, d) P45 surface, and e) P25 surface. The videos (Videos S1–S5, respectively) of the condensation processes on these surfaces can be found in the Supporting Information. 1k× magnification in (a,d); 800× magnification in (b,c,e).

the MG/SiNW surfaces can be clearly identified from the early stages of the condensation processes (see Figure 2c-1,d-1,e-1). The nucleation sites on the plain silicon surface and SiNW surface are randomly distributed, whereas they are aligned at the patterned grooves on the MG/SiNW surfaces. Furthermore, the nucleation site density on the MG/SiNW surfaces can also be manipulated by tailoring the groove density, provided that the nucleation density increases as P decreases from 85 μm to 45 μm and 25 μm, respectively, as shown in Figure 2c-1,d-1,e-1. The videos of the condensation processes are provided in the Supporting Information (Videos S1–S5 for the condensation processes on the plain silicon, SiNW, P85, P45, and P25 surfaces, respectively). It is noted that the charging of electron on the sample surfaces in the ESEM may affect condensation. The effect has been examined by scanning the sample surfaces by electron gun under high vacuum with different durations before releasing water vapor into the ESEM chamber. The obtained condensation images under various scanning durations on the plain silicon, SiNW and P85 surfaces are shown in Figure S2 in the Supporting Information. From the figure, it is found that the effect of charging can be neglected when the electron scanning duration is smaller than 5 min. In the current study, the ESEM images were obtained with a scanning duration shorter than 1 min and therefore the charging effect in current study can be neglected. The electron charging could reduce the nucleation site density on SiNW and MG/SiNW surfaces and enhance wettability on the plain silicon surface. The underlying mechanism causing these phenomena needs to be further investigated.

2.2. The Out-of-Plane Motion of Liquid Droplets

Although condensates on a cooling surface are commonly removed by the gravitational force, spontaneous droplet removal on superhydrophobic surfaces has been observed.[27–30] An out-of-plane motion of liquid droplets was observed on superhydrophobic surfaces.[27–30] The out-of-plane motion of

liquid droplets is attributed to the release of surface free energy when droplets coalesce on the superhydrophobic surface.[27,30] It provides an additional condensate removal mechanism and may enhance the shedding of liquid droplets. The out-of-plane motion of liquid droplets was also observed on the SiNW surface (see Figure 2b-4,b-5) and on the MG/SiNW surfaces (see Figure 2c-2,c-3,d-3,d-4,e-2,e-3). The out-of-plane motions of these liquid droplets were observed because the droplets at the locations downstream of the vanished droplets were unaltered. This suggests that the vanished droplets were not removed by gravity.

2.3. The Underlying Mechanism for the Spatial Control of Nucleation

Nucleation is the first step of phase transitions. Classical nucleation theory (CNT) predicts the nucleation rate from the free energy barrier for the formation of the microscopic nuclei (see, e.g., in the literature).[4] The nucleation theory has been dominated by CNT for nearly a century as developed by Volmer and Weber,[31] Farkas,[32] Becker and Doring,[33] Frenkel,[34] and Zeldovich.[35] In the 1980s, several experiments revealed deviations of the nucleation rate from that predicted by CNT.[36–41] Later modifications show better agreement,[42,43] but the predictions still under predicted by several orders of magnitude.[44] Molecular approaches such as molecular dynamics simulation[45–47] and density functional theory[48,49] can be applied to predict nucleation rates for noble atoms but fail for complex molecules. For a complete review of homogeneous nucleation theories, readers are referred to Oxtoby and colleagues,[50] Laaksonen,[51] Kashchiev,[52] and Vehakmaki.[53] For heterogeneous nucleation, Volmer developed the first model for heterogeneous nucleation by assuming the impurity or substrate surface is a locally plan surface upon which liquid grows.[54] Based on CNT, Fletch proposed a model considering the effect of seed size on nucleation rate.[55] A complete review about heterogeneous nucleation theories can be found in.[52,53] Using Fletch's model, Kashchiev showed that the nucleation rate increases with increasing seed particle size and it becomes saturated when the size of the seed gets bigger.[52] The size dependent nucleation rate is because the nucleus on smaller seeds gives higher free energy barrier for its formation.[52] Following the same reason, it is argued that a concave substrate surface gives higher nucleation rate as compared to convex and flat surfaces.[52] Theoretical studies of nucleation on micro- or nanostructured surfaces have been conducted.[56–60] Liu et al.,[56] Ruckenstein and Berim,[59] and Maksimor et al.[60] also found that concave cavities can promote nucleation. CNT has been modified for finding the nucleation rate in nanocavities.[57–60] However, these models cannot be directly applied to the current study because of the unknown values of line tension or intermolecular potentials in the models. As pointed out by Vehakmaki in 2006 that the prediction of nucleation rates for real substances is either impossible due to lack of realistic interaction models between molecules, or enormous computation costs.[53] At present, this situation still exists. As a consequence, classical nucleation theory (e.g., in another work)[4] is adopted for a qualitative understanding of the observed phenomena in this study.

The preferential droplet nucleation on the aligned MGs on the SiNW surface occurred because the MGs can provide a large number of sizable cavities with a smaller free energy barrier to nucleation compared to that required on the intervals between the NWs, where the sizes of the cavities in the MGs are in the order of a few micrometers, whereas the intervals between the NWs are approximately 200 nm. The free energy barrier to nucleation can be approximated as[4]

$$\Delta G = \frac{4}{3}\pi r_e^2 \sigma_{lv} F - 4\pi \sigma_{lv} F (r_c - r_e)^2 \quad (1)$$

where $F = 0.25(2 - 3\cos\theta + \cos^3\theta)$ and r_e, σ_{lv}, r_c, and θ are the equilibrium radius of droplet, surface tension between liquid/vapor, cavity radius and contact angle, respectively. The equilibrium radius can be obtained using the equation combining Kelvin and Clapeyron effects

$$r_e = \frac{2 v_l \sigma_{lv} T_w}{h_{lv}(T_{sat}(P_v) - T_w)} \quad (2)$$

where v_l, T_w, T_{sat}, P_v, and h_{lv} are liquid specific volume, wall temperature, saturation temperature, vapor pressure, and latent heat, respectively. The equilibrium droplet radius determined from the Kelvin and Clapeyron equation is 3.2 nm. The free energy barrier (ΔG) has a maximal value at r_e, indicating an unstable equilibrium at r_e, and decreases with r_c when r_c is larger than r_e. Using the equation of ΔG with a contact angle of 145° and the obtained equilibrium radius, the free energy barriers to nucleation on cavities in the MGs and on the interval between NWs with r_c equal to 4 μm and 200 nm, respectively, are -1.1×10^{-11} J and -2.8×10^{-14} J, respectively. Consequently, a large number of embryos were observed at the cavities in the MGs as shown in the ESEM image of **Figure 3**a. The embryos grew (Figure 3b), and consequently coalesced, resulting in a medium-size droplet (Figure 3c). The medium-size droplet was absorbed by the adjacent large droplet and new embryo nucleation occurred in this area (Figure 3d). The small embryos next to the large droplet were also the feeding seeds that provided liquid to nourish the large droplet nearby (see Video S6 in the Supporting Information). Conversely, although cavities with sizes in the order of μm occurred in the NW array because of the surface tension effect during the drying of NWs in NW synthesis, their numbers were relatively limited. Therefore, although a liquid droplet can nucleate on the cavity in the NW array, no embryos surrounded the droplet to maintain its growth. Consequently, the droplet size remains relatively unchanged in contrast to the rapid growth of the liquid droplet at the MGs in the observed period (see Figure 3 and the Video S6 in the Supporting Information).

2.4. Quantitative Analysis of the Condensation Processes

2.4.1. Nucleation Site Density and Departure Diameter

The condensation processes on the plain silicon, SiNW, P85, P45, and P25 surfaces were also quantitatively analyzed by examining the nucleation site density (NSD), departure diameter, droplet radius as a function of time, and DWC cycle time on the surfaces; the results are shown in **Figure 4**a–d,

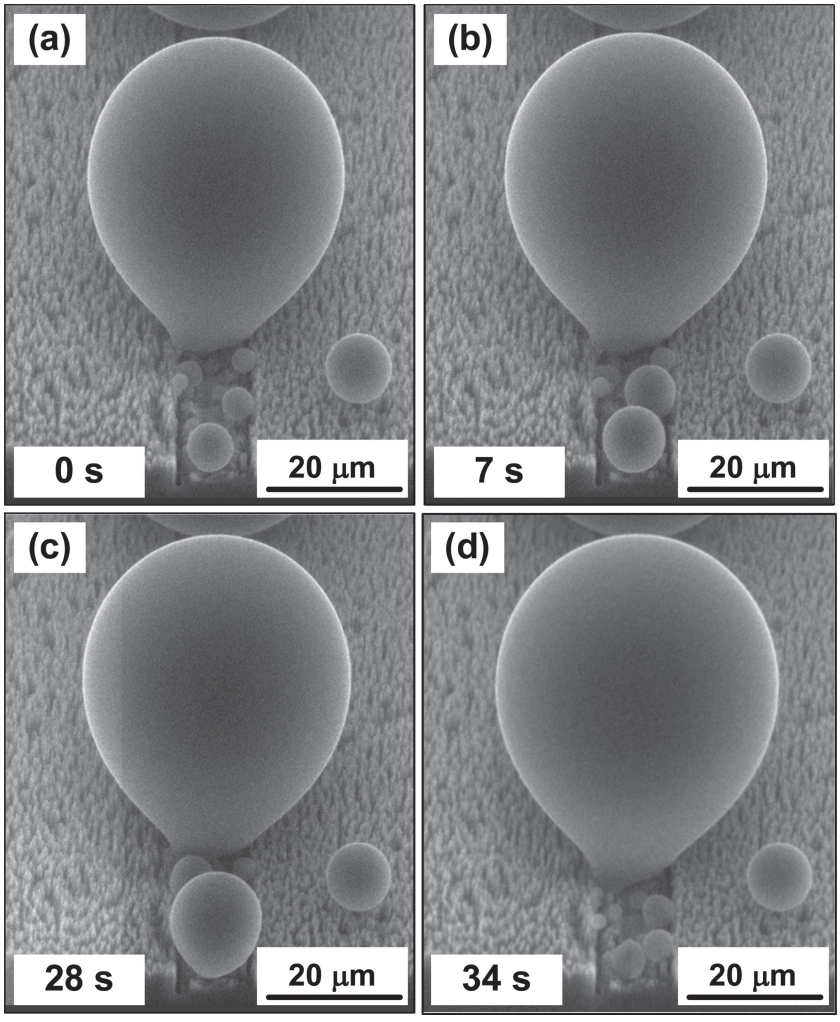

Figure 3. ESEM images (3k× magnification and 15 kV acceleration voltage) of nucleation and droplet growth at the microgrooves on the SiNW surface: a) nucleation of embryos at the cavities in the microgrooves; b) growth of the embryos; c) coalescence of the embryos; d) absorption of the medium-size droplet by the adjacent large droplet and new embryo nucleation occurred in the area.

respectively. At least three repeated experiments were conducted on the surfaces to evaluate the average values shown in Figure 4a–d and the error bars in the figures represent the standard errors. Figure 4a shows the NSD on the surfaces determined from the first recordable ESEM image (i.e., the first row in Figure 2). The NSD was obtained by counting the number of droplets in a fixed area (approximately 340 μm × 180 μm). The NSD on the plain silicon, SiNW, P85, P45, and P25 surfaces are 0.54 ± 0.08, 2.66 ± 0.96, 1.13 ± 0.06, 1.38 ± 0.11, and 3.42 ± 0.10 × 10^9 m^{-2}, respectively. The plain silicon surface has the lowest NSD, whereas the NSD increases with increasing groove density on the MG/SiNW surfaces. The departure diameter of the liquid droplets on the surfaces is shown in Figure 4b. The departure diameter on the plain silicon surface was too large to be recorded by the ESEM. Thus, it was estimated from a theoretical calculation based on the balance of the gravitational force and the surface tension force applied on the droplet on the plain silicon surface (see Figure S3 in Supporting Information for details). The departure diameters on the SiNW and MG/SiNW surfaces were determined by averaging the diameters of droplets shown in the ESEM images at the time before merging of the droplets and immediately departure of the merged droplet occurred. The calculated departure diameter on the plain silicon surface was approximately 7.8 mm, whereas the departure diameters on the SiNW and MG/SiNW surfaces determined from the ESEM images were approximately 100 μm. The same departure diameter on the SiNW and MG/SiNW surfaces indicates that the removal of the droplets on the surfaces is independent of the micro-roughness scale on the surfaces and is only a function of the macroscopic contact angle.

2.4.2. The Evolution of the Liquid Droplets

The evolution of the droplets on the surfaces was also examined as shown in Figure 4(c). The growth of liquid droplets on the surfaces can be generally classified into three regimes. The exponents (α) of the growth rate ($r \propto t^{\alpha}$) are summarized in **Table 1**. In the first regime, no coalescence of liquid droplets was observed, and the exponents (α) of the growth rate on these surfaces were in-between 0.37 and 0.41 for the surfaces, which is close to the 1/3 power law.[22,61–64] The transition from the first regime to the second regime, in which the growth of the liquid droplet is attributed to isolated droplet growth and coalescence of liquid droplets, was observed on the surfaces, and increased the α values to 0.51, 1.38, 0.59, 0.68, and 1.27 on the plain silicon, SiNW, P85, P45, and P25 surfaces, respectively. A continuous transition from the second to the third regime, in which the growth of the liquid droplet is dominated by the coalescence of large liquid droplets, was observed on the plain silicon, SiNW, and P45 surfaces, resulting in high α values of 3.97, 1.23, and 3.63 on the plain silicon, SiNW, and P45 surfaces, respectively. The large NSDs on the SiNW and MG/SiNW surfaces result in an earlier transition from the first to the second regime on these surfaces than that on the plain silicon surface, given that a large droplet growth rate was observed on the SiNW and MG/SiNW surfaces.

2.4.3. The Cycle Time

The cycle time defined as the time required for finishing a cycle from droplet nucleation to droplet departure is shown in Figure 4(d). A smaller cycle suggests a higher heat and mass transfer performance because the process of sweeping and renewal of liquid droplets is responsible for the high performance of DWC. The cycle time for the plain silicon surface

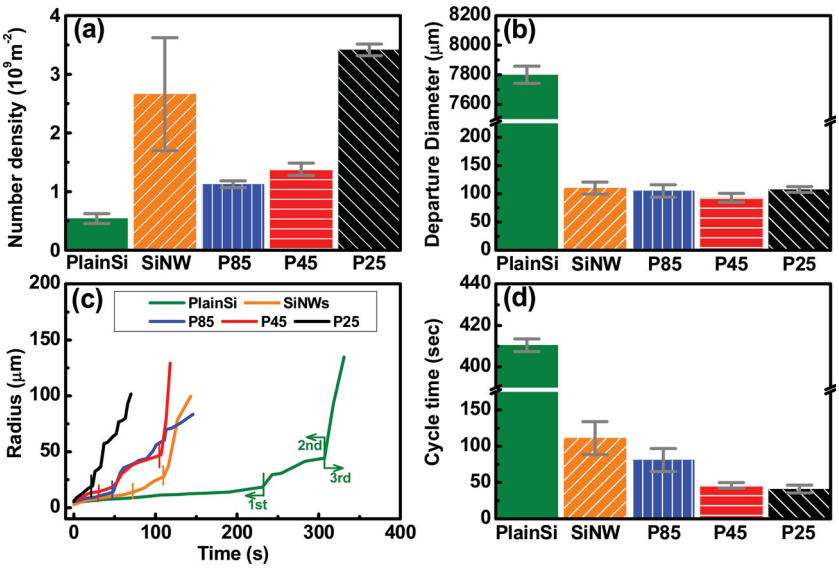

Figure 4. Quantitative analysis of the condensation processes on the surfaces: a) NSD; b) departure diameter; c) droplet radius as a function of time, and d) cycle time.

was estimated from the previous calculated departure diameter and the growth rate of the droplet on the surface (Table 1 and Figure 4c). The cycle times on the plain silicon, SiNW, P85, P45, and P25 surfaces are 410 ± 3 s, 111 ± 23 s, 81 ± 16 s, 46 ± 4 s, and 41 ± 5 s, respectively. The large contact angle and small contact angle hysteresis on the SiNW and MG/SiNW surfaces (see Figure S1 in the Supporting Information) might be responsible for the small cycle times obtained on these surfaces. The MG/SiNW surfaces had a smaller cycle time than that on the SiNW surface because of the earlier transitions from the first to the second regime observed on the surfaces. In addition, the cycle time decreased with increasing groove density on the MG/SiNW surfaces and the P25 surface exhibited the optimal condensate shedding ability among the surfaces. The cycle time on the P25 surface was approximately ten times smaller than that on the plain silicon surface. The small cycle time suggests a high water removal rate on the MG/SiNW surfaces. It is worth noting that the aging effect is insignificant on the studied surfaces because the SiNW and MG/SiNW surfaces are capable for enhancing nucleation and the spatial control of nucleation on MG/SiNW surface are functional for a long period of time of about seven months.

Table 1. The exponents (α) of the growth rate power law ($r \propto t^{\alpha}$) on various surfaces.

Sample ID	Regime 1	Regime 2	Regime 3
Plain Si	0.40	0.51	3.97
SiNW	0.41	1.38	1.23
P85	0.37	0.59	-
P45	0.38	0.68	3.63
P25	0.38	1.27	-

3. Conclusions

In conclusion, this is the first study to demonstrate the ability to spatially control heterogeneous nucleation with rapid and continuous shedding of the condensate on the superhydrophobic surface. The control was achieved by engineering the free energy barrier to nucleation by parameterizing regional roughness scales on the superhydrophobic SiNW array-coated surface. Liquid droplets preferentially nucleate on the microgrooves on the NW array-coated surfaces. The nucleation site density can also be manipulated by tailoring the number of grooves on the surface. The small cycle time obtained on the MG/SiNW surfaces suggests potentially high heat and mass transfer rates on the surfaces. The ability of spatial control of heterogeneous nucleation with a rapid and continuous shedding of the condensate paves the way towards manipulating the daily phenomenon of condensation. The insights from the study can have implications in enhancing efficiencies in a wide range of industrial systems, prompting water harvesting, as well as can alleviate local hot spots in electronic devices.

4. Experimental Section

The Detail for Conducting Condensation Experiments in the ESEM Chamber: The test section for conducting the condensation experiments in the ESEM chamber is shown in Figure S4 in the Supporting Information. The condensation samples with dimensions of 4 mm × 2 mm × 500 μm and a nanowire (NW) array on top of the surfaces were attached to the surface of the cooling stage with a tilted angle of 45° using a carbon tape. The condensation experiments were conducted under a controlled condition in which the wall temperature was maintained at 0 ± 0.2 °C and the pressure of the chamber was constant at 6 Torr (corresponding to water saturation temperature of 3.91 °C).

Fabrication of the Silicon Nanowire Array-Coated Surfaces with Microgrooves: The method of SiNW array synthesis is similar to previous studies.[65–67] The method is shown in Figure S5 in the Supporting Information and is described as follows: A silicon wafer is immersed into an aqueous solution of $AgNO_3$ and HF acid. Ag^+ in the solution reduces to Ag by oxidizing the surrounding silicon on the wafer surface. The oxidized area surrounding the Ag nanoparticles is subsequently etched by HF. After successive oxidation and etching, a nanowire array and a dendrite structure of Ag on the top the nanowires form on the surface. The dendrite structure is removed by HNO_3 etching and a free standing silicon nanowire array can be obtained. The fabrication procedure for the silicon nanowire array-coated surfaces with microgrooves is shown in Figure S6 in the Supporting Information. The fabrication process is briefly described as follows: A thin layer of SiNx with thickness of approximately 450 nm was deposited using a low pressure chemical vapor deposition process and a layer of photoresist (PR) was spin-coated and patterned on top of the SiNx layer. The exposed SiNx was etched away using reactive ion etching (RIE), followed by the removal of the PR layer. The remaining SiNx layer served as an etching mask for silicon etching and microgrooves were obtained using an anisotropic KOH (30 %) etching. The SiNx layer was subsequently removed using RIE. The surface with mircogrooves on the silicon nanowire array was obtained by immersing the whole wafer into a solution containing HF and $AgNO_3$ nanoparticles.

The superhydrophobic silicon nanowire array with microgrooves was obtained by coating a thin layer of polytetrafluoroethylene (approximately 20 nm) on top of the silicon nanowire array.

Supporting Information

Supporting Information is available from the Wiley Online Library or from the author.

Acknowledgements

The authors thank the Institute of Cellular and Organismic Biology at Academia Sinica in Taiwan for the use of the ESEM. The authors also thank the Nano Facility Center at National Chiao Tung University for use of their facilities. This work was supported by the National Science Council of Taiwan under grant No. NSC 101-2221-E-009 -042.

Received: June 10, 2013
Revised: August 16, 2013
Published online: October 25, 2013

[1] H. Z. Kister, *Distillation Design*, McGraw-Hill Education, New York, USA **1992**.
[2] H. G. Andrews, E. A. Eccles, W. C. E. Schofield, J. P. S. Badyal, *Langmuir* **2011**, *27*, 3798.
[3] Y. A. Cengel, M. A. Boles, *Thermodynamics: An engineering approach*, McGraw-Hill, New York, USA **2008**.
[4] V. P. Carey, *Liquid-Vapor Phase-Change Phenomena*, Taylor and Francis, New York, USA **2008**.
[5] F. P. Incropera, D. P. Dewitt, T. L. Bergman, A. S. Lavine, *Foundations of Heat Transfer*, John Wiley and Sons, Singapore **2013**.
[6] A. B. D. Cassie, S. Baxter, *Trans. Faraday Soc.* **1944**, *40*, 546.
[7] R. N. Wenzel, *Ind. Eng. Chem.* **1936**, *28*, 988.
[8] E. Schmidt, W. Schurig, W. Sellschopp, *Tech. Mech. Thermodyn.* **1930**, *1*, 11.
[9] M. Nosonovsky, B. Bhushan, *Multiscale Dissipative Mechanisms and Hierarchical Surfaces: Friction, Superhydrophobicity and Biomimetics*, Springer-Verlag Berlin Heidelberg, Berlin, Heidelberg, Germany **2008**.
[10] C. Dorrer, J. Rühe, *Soft Matter* **2009**, *5*, 51.
[11] T. Koishi, K. Yasuoka, S. Fujikawa, T. Ebisuzaki, X. C. Zeng, *Proc. Natl. Acad. Sci.* **2009**.
[12] A. Nakajima, K. Hashimoto, T. Watanabe, *Monatsh. Chem.* **2001**, *132*, 31.
[13] X. Zhang, F. Shi, J. Niu, N. Jiang, Z. Wang, *J. Mater. Chem.* **2008**, *18*, 621.
[14] A. Lafuma, D. Quéré, *Nat. Mater.* **2003**, *2*, 457.
[15] R. BLOSSEY, *Nat. Mater.* **2003**, *2*, 6.
[16] D. Quéré, *Rep. Prog. Phys.* **2005**, *68*, 2495.
[17] Q. Zheng, C. Lv, P. Hao, J. Sheridan, *Sci. China Phys. Mech. Astron.* **2010**, *53*, 2245.
[18] R. Narhe, D. Beysens, *Phys. Rev. Lett.* **2004**, *93*.
[19] K. A. Wier, T. J. McCarthy, *Langmuir* **2006**, *22*, 2433.
[20] Y. C. Jung, B. Bhushan, *J . Micros c.* **2008**, *229*, 127.
[21] C.-H. Chen, Q. Cai, C. Tsai, C.-L. Chen, G. Xiong, Y. Yu, Z. Ren, *Appl. Phys. Lett.* **2007**, *90*, 173108.
[22] X. Chen, J. Wu, R. Ma, M. Hua, N. Koratkar, S. Yao, Z. Wang, *Adv. Funct. Mater.* **2011**, *21*, 4617.
[23] J. Cheng, A. Vandadi, C.-L. Chen, *Appl. Phys. Lett.* **2012**, *101*, 131909.
[24] K. K. Varanasi, M. Hsu, N. Bhate, W. Yang, T. Deng, *Appl. Phys. Lett.* **2009**, *95*, 094101.
[25] W. Li, A. Amirfazli, *J. Colloid Interface Sci.* **2005**, *292*, 195.
[26] W. Li, A. Amirfazli, *Adv. Colloid Interface Sci.* **2007**, *132*, 51.
[27] J. Boreyko, C.-H. Chen, *Phys. Rev. Lett.* **2009**, *103*.
[28] K. Rykaczewski, A. T. Paxson, S. Anand, X. Chen, Z. Wang, K. K. Varanasi, *Langmuir* **2013**, *29*, 881.
[29] C. Dorrer, J. Rühe, *Adv. Mater.* **2008**, *20*, 159.
[30] N. Miljkovic, R. Enright, Y. Nam, K. Lopez, N. Dou, J. Sack, E. N. Wang, *Nano Lett.* **2013**, *13*, 179.
[31] M. Volmer, A. Weber, *Z. Phys. Chem.* **1925**, *119*, 277.
[32] L. Farkas, *Z. Phys. Chem.* **1927**, *125*, 236.
[33] V. R. Becker, W. Doring, *Ann. Phys.* **1935**, *24*, 719.
[34] J. Frenkel, *J. Chem. Phys.* **1939**, *7*, 538.
[35] J. B. Zeldovich, *Zh. Eksp. Teor. Fiz.* **1942**, *12*, 525.
[36] P. E. Wagner, R. Strey, *J. Phys. Chem.* **1981**, *85*, 2694.
[37] R. C. Miller, *J. Chem. Phys.* **1983**, *78*, 3204.
[38] P. E. Wagner, R. Strey, *J. Chem. Phys.* **1984**, *80*, 5266.
[39] G. W. Adams, J. L. Schmitt, R. A. Zalabsky, *J. Chem. Phys.* **1984**, *81*, 5074.
[40] A. Kacker, R. H. Heist, *J. Chem. Phys.* **1985**, *82*, 2734.
[41] R. Strey, P. E. Wagner, T. Schmeling, *J. Chem. Phys.* **1986**, *84*, 2325.
[42] S. L. Girshick, C.-P. Chiu, *J. Chem. Phys.* **1990**, *93*, 1273.
[43] H. Reiss, W. K. Kegel, J. L. Katz, *J. Phys. Chem.* **1998**, *102*, 8548.
[44] J. Wolk, R. Strey, *J. Phys. Chem. B* **2001**, *105*, 11683.
[45] P. R. ten Wolde, D. Frenkel, *J. Phys. Chem.* **1998**, *109*, 9901.
[46] K. Laasonen, S. Wonczak, R. Strey, A. Laaksonen, *J. Phys. Chem.* **2000**, *113*, 9741.
[47] S. Toxvaerd, *J. Phys. Chem.* **2001**, *115*, 8913.
[48] X. C. Zeng, D. W. Oxtoby, *J. Phys. Chem.* **1991**, *94*, 4472.
[49] V. Talanquer, D. W. Oxtoby, *J. Phys. Chem.* **1994**, *100*, 5190.
[50] D. W. Oxtoby, *J. Phys.: Condensed Matter* **1992**, *4*, 7627.
[51] A. Laaksonen, V. Talanquer, D. W. Oxtoby, *Ann. Rev. Phys. Chem.* **1995**, *46*, 489.
[52] D. Kashchiev, *Nucleation: Basic Theory with Applications*, Butterworth-Heinemann, Oxford, UK **2000**.
[53] H. Vehkamaki, *Classical Nucleation Theory in Multicomponent Systems*, Springer-Verlag Berlin Heidelberg, Berlin, Heidelberg, Germany **2006**.
[54] M. Volmer, *Z. Elektrochem* **1929**, *35*, 555.
[55] N. H. Fletcher, *J. Chem. Phys.* **1958**, *29*, 572.
[56] Q. Liu, Y. Zhu, G. Yang, Q. Yang, *J. Mater. Sci. Technol.* **2008**, *24*, 183.
[57] V. G. Dubrovskii, M. V. Nazarenko, N. V. Sibirev, *Tech. Phys. Lett.* **2009**, *35*, 1117.
[58] A. O. Maksimov, A. M. Kaverin, *Tech. Phys. Lett.* **2010**, *36*, 872.
[59] E. Ruckenstein, G. O. Berim, *J. Colloid Interface Sci.* **2010**, *351*, 277.
[60] A. O. Maksimov, A. M. Kaverin, V. G. Baidakov, *Langmuir* **2013**, *29*, 3924.
[61] J. Viovy, D. Beysens, C. Knobler, *Phy. Rev. A* **1988**, *37*, 4965.
[62] A. Steyer, P. Guenoun, D. Beysens, C. Knobler, *Phy. Rev. A* **1991**, *44*, 8271.
[63] M. Ichikawa, N. Magome, K. Yoshikawa, *Europhys. Lett.* **2004**, *66*, 545.
[64] R. D. Narhe, D. A. Beysens, *Langmuir* **2007**, *23*, 6486.
[65] K. Q. Peng, Y. J. Yan, S. P. Gao, *Adv. Mater.* **2002**, *14*, 1164.
[66] R. Chen, M.-C. Lu, V. Srinivasan, Z. Wang, H. H. Cho, A. Majumdar, *Nano Lett.* **2009**, *9*, 548.
[67] M.-C. Lu, R. Chen, V. Srinivasan, V. P. Carey, A. Majumdar, *Int. J. Heat Mass Tran.* **2011**, *54*, 5359.